

This work was written as part of one of the author's official duties as an Employee of the United States Government and is therefore a work of the United States Government. In accordance with 17 U.S.C. 105, no copyright protection is available for such works under U.S. Law. Access to this work was provided by the University of Maryland, Baltimore County (UMBC) ScholarWorks@UMBC digital repository on the Maryland Shared Open Access (MD-SOAR) platform.

Please provide feedback

Please support the ScholarWorks@UMBC repository by emailing [scholarworks-group@umbc.edu](mailto:scholarworks-group@umbc.edu) and telling us what having access to this work means to you and why it's important to you. Thank you.

## HUNTING FOR TREASURES AMONG THE *FERMI* UNASSOCIATED SOURCES: A MULTIWAVELENGTH APPROACH

F. ACERO<sup>1</sup>, D. DONATO<sup>2</sup>, R. OJHA<sup>1,3,4,8,9</sup>, J. STEVENS<sup>5</sup>, P. G. EDWARDS<sup>6</sup>, E. FERRARA<sup>2</sup>,  
J. BLANCHARD<sup>4</sup>, J. E. J. LOVELL<sup>4</sup>, AND D. J. THOMPSON<sup>7</sup>

<sup>1</sup> ORAU/NASA Goddard Space Flight Center, Astrophysics Science Division, Code 661, Greenbelt, MD 20771, USA; [fabio.f.acero@nasa.gov](mailto:fabio.f.acero@nasa.gov)

<sup>2</sup> CRESST/NASA Goddard Space Flight Center, Astrophysics Science Division, Code 661, Greenbelt, MD 20771, USA

<sup>3</sup> The Catholic University of America, 620 Michigan Avenue, N.E., Washington, DC 20064, USA

<sup>4</sup> University of Tasmania School of Mathematics & Physics, Private Bag 37, Hobart TAS 7001, Australia

<sup>5</sup> CSIRO Astronomy and Space Science, Locked Bag 194, Narrabri NSW 2390, Australia

<sup>6</sup> CSIRO Astronomy and Space Science, P.O. Box 76, Epping NSW 1710, Australia

<sup>7</sup> NASA Goddard Space Flight Center, Astrophysics Science Division, Code 661, Greenbelt, MD 20771, USA

Received 2013 June 15; accepted 2013 October 4; published 2013 December 3

### ABSTRACT

The *Fermi* Gamma-Ray Space Telescope has been detecting a wealth of sources where the multiwavelength counterpart is either inconclusive or missing altogether. We present a combination of factors that can be used to identify multiwavelength counterparts to these *Fermi* unassociated sources. This approach was used to select and investigate seven bright, high-latitude unassociated sources with radio, UV, X-ray, and  $\gamma$ -ray observations. As a result, four of these sources are candidates to be active galactic nuclei, and one to be a pulsar, while two do not fit easily into these known categories of sources. The latter pair of extraordinary sources might reveal a new category subclass or a new type of  $\gamma$ -ray emitter. These results altogether demonstrate the power of a multiwavelength approach to illuminate the nature of unassociated *Fermi* sources.

**Key words:** galaxies: active – gamma rays: general – pulsars: general – quasars: general – radio continuum: galaxies – ultraviolet: galaxies – X-rays: galaxies

**Online-only material:** color figures, machine-readable table

### 1. INTRODUCTION

The ongoing survey of the  $\gamma$ -ray sky with the *Fermi* Large Area Telescope (LAT) has led to a tremendous increase in the known population of  $\gamma$ -ray sources. The two-year *Fermi* LAT catalog (2FGL; Nolan et al. 2012) lists 1873 sources, divided into the following classes: (1) active galactic nuclei (AGNs;  $\sim 60\%$ ); (2) pulsars and binary systems (6%); (3) supernova remnants, pulsar wind nebulae, and other Galactic sources (4%); and (4) unassociated sources ( $\sim 30\%$ ). Thus, the second largest “class” consists of sources that do not have a clear association with plausible counterparts at other wavelengths. At the very least, this large number of mysterious  $\gamma$ -ray sources includes outliers of known classes of sources. It is not unreasonable to suppose that a subset of these sources could provide a pathway to new discoveries.

The unassociated sources in the 2FGL catalog at high Galactic latitude ( $|b| > 5^\circ$ ) are likely to fall under two main categories: AGNs or millisecond pulsars (MSPs). The members of each category share characteristic  $\gamma$ -ray properties that can be used as patterns to evaluate the probability of a given source to belong to a class of objects (e.g., Ackermann et al. 2012; Mirabal et al. 2012). The typical  $\gamma$ -ray signatures of an AGN are nonperiodic variability and a power law or broken power law spectral shape (see, e.g., the second *Fermi* LAT catalog of AGNs; Ackermann et al. 2011). For pulsars and MSPs, the key to identification is the detection of pulsations in  $\gamma$ -rays. Furthermore, their spectra are usually curved and present a cutoff around a few GeV (see, e.g., the first *Fermi* pulsar catalog; Abdo et al. 2010a).

Although the source localization accuracy made possible by the *Fermi* LAT has greatly improved over previous  $\gamma$ -ray instruments, the typical 95% confidence level position uncertainty radius ( $R_{95}$ ) of 2FGL sources is of the order of  $\sim 0.1^\circ$ , which is still relatively large with respect to lower energy positional errors to make associations solely based on the  $\gamma$ -ray position.

To resolve this issue, multiwavelength campaigns can be decisive in revealing the nature of some *Fermi* unassociated sources. For example, the deep search for radio pulsations at  $\gamma$ -ray positions has led to the discovery of unexpectedly large numbers of pulsars and MSPs (Ray et al. 2012) in the population of  $\gamma$ -ray unassociated sources.

In addition, X-rays are very good tracers of energetic processes, and above a few keV they are not affected by absorption along the line of sight. From the observational point of view, the current X-ray satellites have relatively large fields of view (FOVs), high sensitivity, and a localization at the arcsec level.

A precise location, derived from the X-rays, can also strongly enhance the sensitivity of  $\gamma$ -ray blind searches for pulsation of isolated pulsars (Dormody et al. 2011) with the *Fermi* LAT by dramatically reducing the numbers of position trials. In the case of an MSP in a binary system, optical observations of the companion are needed to obtain the orbital period of the system (see Romani 2012, for a recent example). However, it is often found that there is more than one plausible X-ray counterpart to a *Fermi* unassociated source. While this number can largely vary depending on the position on the sky and the characteristics of the telescope, Cheung et al. (2012), for example, found  $\sim 10$  sources with the *Chandra* X-ray telescope (XRT) in the error ellipses of the two brightest 0FGL unassociated sources 0FGL J1311.9–3419 and 0FGL J1653.4–0200. In those cases,

<sup>8</sup> Adjunct Professor.

<sup>9</sup> Honorary Fellow.

the high spatial resolution and large frequency range provided by radio interferometry can provide a crucial step in identifying the counterpart. Observations at multiple radio frequencies are useful as they can indicate the nature of the object identified, e.g., relatively high compact radio flux density and a flat radio spectrum suggest the object could be an AGN. Once a potential AGN counterpart has been identified, optical follow-up to search for a redshift and optical polarization will provide another strong piece of evidence. Unambiguous identification is made when correlated variability is observed in  $\gamma$ -rays at another wavelength. The identification of *Fermi* unassociated sources with known classes of astrophysical objects is of interest, not least because these new identifications often constitute a new population, e.g., AGN identifications might discover a subclass of radio-weak,  $\gamma$ -ray loud objects.

On a population scale, several groups (see, e.g., Ackermann et al. 2012; Mirabal et al. 2012) have developed methods to try to predict the nature of a *Fermi* unassociated source on the basis of a subset of its  $\gamma$ -ray features that were found to be effective at discriminating between AGNs and pulsars. Mirabal et al. (2012), for example, used the spectral and variability information about the LAT sources to assign a probability  $P(\text{AGN})$  that an unassociated source is an AGN. Other approaches have studied the lower wavelength counterparts to the  $\gamma$ -ray sources. For example, Massaro et al. (2012a, 2012b) have developed a method to identify the AGN candidates among the 2FGL unassociated sources on the basis of the colors of the infrared counterparts lying within the *Fermi* error ellipse by using the all-sky survey from the *Wide-field Infrared Survey Explorer* (*WISE*).

While the largest class of predicted sources from all these methods is the AGN, some sources did not fit in the AGN or pulsar category and were considered “unclassifiable” or “outlier objects.” It is vital to make these identifications so that the properties of these truly “exotic” *Fermi* unassociated sources can be studied.

## 2. DESCRIPTION OF THE METHOD

### 2.1. Selection of *Fermi* LAT Sources

To limit number of potential multiwavelength counterparts to explore, we selected bright unassociated  $\gamma$ -ray sources (average significance in all energy bands given in the 2FGL  $\sigma > 10$ ), as these usually have smaller position uncertainty. We selected sources located at high latitudes ( $|b| > 5^\circ$ ) where the density of potential counterparts is lower. We removed all unassociated sources labeled as “c” in 2FGL (those found in a region with bright and/or possibly incorrectly modeled diffuse emission). Those different selection criteria reduced the sample of unassociated *Fermi* sources in the 2FGL from 555 to 85 ( $\sigma > 10$ ), then 33 ( $|b| > 5^\circ$ ), and finally 32 (no “c” flag).

Among this sample of bright, high-latitude, unconfused unassociated 2FGL targets, we selected the sources that had been observed in the X-rays by the *Swift* satellite, whose XRT FOV typically encompasses the *Fermi* uncertainty ellipse. We excluded sources observed by other recent X-ray missions (i.e., *XMM*, *Suzaku*, and *Chandra*) because these data sets have already been studied extensively. In 2010, *Swift* began a systematic search<sup>10</sup> for X-ray counterparts of *Fermi* LAT unassociated sources (see Stroh & Falcone 2013). For this reason, the large

majority of those bright, high-latitude unassociated 2FGL targets have X-ray coverage. We selected only observations with at least a 3.5 ks exposure time. Our final list includes 22  $\gamma$ -ray sources.

### 2.2. Identification of X-Ray Counterparts

The *Swift* observations were analyzed (see Section 3.1) to identify potential X-ray counterparts within the *Fermi*  $R_{95}$  error ellipse. Among the 22  $\gamma$ -ray sources, 16 had at least one X-ray counterpart detected with a significance greater than  $3\sigma$ . The remaining six  $\gamma$ -ray sources<sup>11</sup> had no X-ray counterpart and represent a puzzling sample that would require deeper X-ray observations. The spatial resolution of the *Swift* XRT (18" half power diameter) allows a localization at the level of a few arcseconds. Once this precise position in the X-ray is obtained, multiwavelength follow-ups with radio, IR, or optical observatories (whose FOVs are typically smaller) are possible.

### 2.3. Radio Follow-up of Potential Counterparts

The combination of X-rays and follow-up radio observations provides a powerful tool to test the two most commonly known scenarios (AGN or pulsar and MSP) for our sample of *Fermi* unassociated sources. Sources that do not show typical characteristics of these two populations are therefore promising candidates for new discoveries.

Multifrequency radio observations of X-ray counterparts are useful to search for radio flat spectrum sources, a typical signature for an AGN. If no radio counterpart to the X-ray source is detected (or is faintly detected only at the lowest radio frequency), the  $\gamma$ -ray source might be a good MSP candidate. Obtaining the precise X-ray positions of the potential counterparts was a key element in optimizing our radio observation strategy. These X-ray positions were used to carry out follow-up observations with the Australia Telescope Compact Array (ATCA) radio telescope and to minimize the number of radio pointings per *Fermi* source. This approach allowed deeper observation of each X-ray counterpart. The typical *Fermi* error ellipse is  $0.1$  in the semimajor axis, and the primary beam of the ATCA radio telescope at the observed frequencies ranges from about 10 arcmin at 5.5 GHz to about 1 arcmin at 40 GHz.

From the list of 16  $\gamma$ -ray sources with at least one X-ray counterpart, radio observations of seven sources were obtained with the ATCA. These objects are presented in Table 1.

## 3. DATA ANALYSIS

### 3.1. X-Rays

We analyzed all the archival clean event files obtained in the photon counting mode by the XRT on board *Swift* and covering the uncertainty ellipse of each  $\gamma$ -ray source. In some cases several exposures of the same  $\gamma$ -ray source have been taken. After combining them within *XSelect*, we used *Ximage* to perform source detection. The resulting images are shown in Figure 1.

We then used those coordinates to run “the *Swift*-XRT data products generator,” available at the University of Leicester Web site,<sup>12</sup> to perform the data reduction and the early data analysis. This facility allowed the creation of (1) three combined event files of all the observations, one in the full energy band

<sup>10</sup> <http://www.swift.psu.edu/unassociated>

<sup>11</sup> 2FGL J0032.7–5521, J0934.0–6231, J1625.2–0020, J1744.1–7620, J2039.8–5620, and J2112.5–3042.

<sup>12</sup> [http://www.swift.ac.uk/user\\_objects/index.php](http://www.swift.ac.uk/user_objects/index.php)

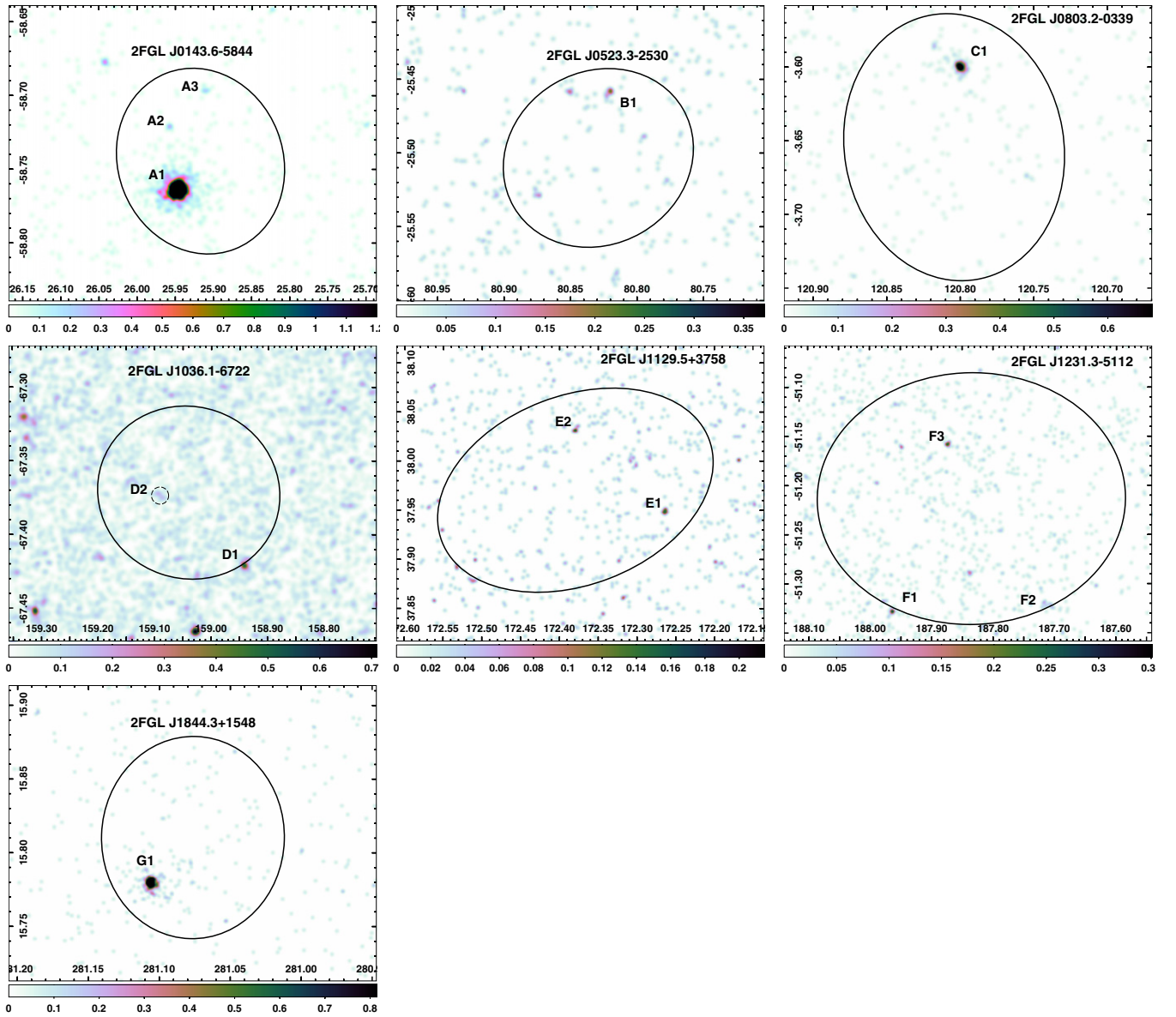


**Figure 1.** *Swift* X-ray count maps (0.3–10 keV energy band) of the selected sample of 2FGL unassociated sources with X-ray coverage and dedicated follow-up radio observations. The black ellipses represent the 95% confidence level position of the *Fermi* source. The X-ray sources presented in Table 1 are labeled on the images. The images are in R.A./decl. coordinates, and the color scale is linear. The images have been smoothed with a Gaussian of 7'' kernel.

(A color version of this figure is available in the online journal.)

**Table 1**  
Multiwavelength Properties of the Observed Sample of 2FGL Unassociated Sources

2FGL Name	J0143.6			J0523.3	J0803.2	J1036.1		J1129.5		J1231.3			J1844.3
$P(\text{AGN})$	1.0			0.738	0.964	-		0.962		0.554			0.996
X-ray name	A1	A2	A3	B1	C1	D1	D2	E1	E2	F1	F2	F3	G1
$\sigma_{\text{det}}$	43.0	3.3	3.0	3.3	9.6	5.6	3.1	3.4	3.0	3.9	3.3	3.6	16.8
$\sigma_{\text{var}}$	4.8	N	N	N	3.5	N	N	N	N	-	-	-	9.1
UV	1--1	1--1	1--1	-0--	-1--	1100	1111	-111	-111	1111	1-1-	1-11	1,1,0--1-
Radio	111100	100000	100000	100000	111110	10----	00----	11----	00----	00----	00----	00----	111111

**Notes.** For each  $\gamma$ -ray source, we report the probability of the source to be an AGN on the basis of its GeV properties (Mirabal et al. 2012), see Section 5 for more details. For each X-ray source within or very close to the  $\gamma$ -ray uncertainty ellipse, we report (1) the label as shown in Figure 1; (2) the detection significance ( $\sigma_{\text{det}}$ ) of the X-ray source; (3) the significance of X-ray variability. When no significant variability was observed ( $\sigma_{\text{var}} < 3$ ) or the variability could not be tested (only one observation available), we used the label *N* and a dash, respectively; (4) the detection of an UV counterpart in the *U*, *W1*, *M2*, and *W2* filters; and (5) the detection of a radio counterpart at 5.5, 9, 17, 19, 38, and 40 GHz. For both the UV and radio rows, “1” and “0” represent a detection and an upper limit, respectively. A dash means that the source was not observed in that specific filter/frequency. The sources A3, B1, and D1 have a faint radio counterpart just above the detection threshold, and although they are not detected at high frequency, a radio flat spectrum is not excluded. The source J1129.5+3758 could not be observed at higher radio frequencies because of its low elevation angle.



0.3–10 keV and two in the sub-bands 0.3–1.5 keV (*S* band) and 1.5–10 keV (*H* band); (2) a combined 0.3–10 keV spectral file for both the source and the background; and (3) a 0.3–10 keV light curve, binned by observation. We used the 0.3–10 keV combined event file to estimate the significance of detection ( $\sigma_{\text{det}}$ ), the combined spectral file to perform a spectral analysis for those sources with a high level of detection significance, the sub-bands event files to estimate the hardness ratios (defined as  $(H - S)/(H + S)$ , where the counts are typically extracted from a 20" circular region) for the less significant sources, and the light curve to check the presence of variability. The wide range of separation between *Swift* snapshots (from a few days to many months) has allowed us to test the X-ray variability of potential, bright counterparts by comparing the X-ray flux in the 0.3–10 keV energy band for each available observation. The significance of the X-ray variability was calculated as  $\sigma_{\text{var}} = (\text{CR}_{\text{max}} - \text{CR}_{\text{min}})/\sqrt{\text{CR}_{\text{min, err}}^2 + \text{CR}_{\text{max, err}}^2}$ , where CR is the net count rate. We note that all the detected sources are within 10 arcmin of the center of the images, where the XRT is best calibrated, and the estimated count rates are not affected by issues at the edges of the CCD. The values of  $\sigma_{\text{var}}$  and  $\sigma_{\text{det}}$  are reported in Table 1 for X-ray sources found within the  $R_{95}$  *Fermi* error ellipse at a detection significance  $> 3\sigma$ . The position of the X-ray sources presented in Section 4.1 were obtained with the task XRTcentroid.

### 3.2. UV and Optical

The Ultraviolet/Optical Telescope (UVOT) provides coverage simultaneous to the XRT by using the UVOT “filter of the day.” This gives us partial, random coverage in the *U*, *W1*, *M2*, and *W2* filters (no observations with *V* or *B* filters were performed). We analyzed the public data by using the standard tools from the *Swift* analysis Web page of HEASARC<sup>13</sup>.

For each filter, we combined all the exposures within a single observation to estimate the monochromatic flux (corrected for the finite aperture of the extraction region, coincidence loss, and large scale sensitivity). For sources with multiple observations, we kept them separated to check for variability in the bright sources. For the dim sources, the observations were combined to increase the signal-to-noise ratio or to lower the upper limit in case of nondetection. We summed both the sky images and the exposure maps by using `uvotimsum`. The photometry has been obtained by running `uvotsource` and using a circular source extraction region (with a radius varying between 3" and 5", depending on the source intensity) and an annular background centered on the source (with an inner radius not less than 15"). In Table 1 we report if the source has been detected in each available filter. The detection threshold in `uvotsource` has been set to the canonical  $3\sigma$ .

### 3.3. Radio

Regular observations with the ATCA are a key component of the TANAMI program (Ojha et al. 2010), which monitors southern hemisphere *Fermi* LAT detected sources at a number of radio frequencies and resolutions. Every few weeks, “snapshot” observations are made at the frequencies 5.5, 9, 17, 19, 38, and 40 GHz, where each frequency is the center of a 2 GHz wide band and the fluxes are calibrated against the ATCA primary flux calibrator PKS 1934–638 (Stevens et al. 2012).

For some candidates, there were multiple X-ray counterparts within the *Fermi* LAT error circle, and in many cases these

**Table 2**  
Multiwavelength Fluxes for the Sources Presented in Figure 2

R.A. (deg)	Decl. (deg)	$\log(\nu)$ (Hz)	$\log(\nu F_{\nu})$ (erg s <sup>-1</sup> cm <sup>-2</sup> )	$\sigma_{\log(\nu F_{\nu})}$ (erg s <sup>-1</sup> cm <sup>-2</sup> )	$\sigma_{\log(\nu)}$ (Hz)
25.94842	-58.76394	8.925828	-15.622386	0.018426	0
25.94749	-58.76427	13.945321	-11.921973	0.011604	0
25.94749	-58.76427	13.814048	-12.033405	0.011605	0
25.94749	-58.76427	13.397592	-12.446089	0.022967	0
25.94749	-58.76427	13.134368	-12.498567	0.116964	0

(This table is available in its entirety in a machine-readable form in the online journal. A portion is shown here for guidance regarding its form and content.)

counterparts were too far from each other to be observed in one pointing of the ATCA. Each observation was for 8 minutes at each band, and the first observation was made at the lowest frequency, where an AGN counterpart would likely have the highest flux density. In cases where no detection was made at the lower frequencies, no observations were made at the higher frequencies.

These positions and error ellipses were obtained by first imaging each source (that had at least some detected flux at 5.5 GHz) in a standard manner using MIRIAD. Because of the elongated beams (in most cases), the beam fitting was done using the task IMFIT. IMFIT was used to obtain the position and error ellipse after checking that the source was realistically extracted from the image.

## 4. RESULTS

The results of our X-ray and radio observational campaigns are described in the following sections. These results are summarized in Table 1, and the UV, radio, and X-ray fluxes are provided in Table 2, which is available in full in the online journal.

### 4.1. *Swift* Results

While some of the  $\gamma$ -ray sources have only one detected counterpart, for the majority of them multiple X-ray counterparts have been found within, or just outside, the  $R_{95}$   $\gamma$ -ray position uncertainty reported in the 2FGL catalog. Only a handful of them have a detection significance above  $5\sigma$ . The typical X-ray uncertainty position is of the order of 3"–6".

Here we report the results of the analysis of the XRT and UVOT instruments. Whenever the statistics were sufficient, a double-absorbed power law model was fitted to the data to derive basic spectral parameters for the sources detected with the XRT. The first absorption corresponds to the Galactic value (from the Leiden/Argentine/Bonn Survey of Galactic H I; Kalberla et al. 2005), and the second is intrinsic to the source and is left free to vary in the fitting. Both absorptions were modeled using the *phabs* model available in XSPEC.

*J0143.6–5844*. In the  $R_{95}$  *Fermi* LAT ellipse we found three X-ray sources in a 4.4 ks exposure. While A2 and A3 (R.A. = 01<sup>h</sup>43<sup>m</sup>49<sup>s</sup>.85; decl. = -58°43'19".2; and R.A. = 01<sup>h</sup>43<sup>m</sup>38<sup>s</sup>.61; decl. = -58°41'50".2) have a low detection significance and are moderately soft (hardness ratio HR = -0.6 and -0.3, respectively), A1 (R.A. = 01<sup>h</sup>43<sup>m</sup>47<sup>s</sup>.57; decl. = -58°45'51".6) is a bright object with 1590 counts. The spectral analysis revealed an absorption along the line of sight in slight excess over the Galactic value ( $n_{\text{H, Gal}} = 2.04 \times 10^{20}$  cm<sup>-2</sup>,  $n_{\text{H, int}} = 3.3_{-0.2}^{+6.5} \times 10^{20}$  cm<sup>-2</sup>) with a photon index  $\Gamma = 2.29 \pm 0.12$ . *Swift* observed the FOV of this  $\gamma$ -ray source three times. While the

<sup>13</sup> <http://heasarc.nasa.gov/docs/swift/analysis/>

hardness ratio of A1 does not change over time (indicating no spectral evolution), the net, corrected count rate varies between  $0.503 \pm 0.024$  and  $0.671 \pm 0.026$ , with a significance of variability of  $\sigma_{\text{var}} \sim 4.8$ . Both the brightness changes and the shape of the spectrum are typical characteristics of an AGN. All three sources were detected at UV frequencies in the *U* and *W2* filters. In the first and last observation, both performed with the *W2* filter, no sign of flux variation is seen for A1, while only one observation was performed with the *U* filter and no variability can be assessed.

*J0523.3–2530*. The only possible X-ray counterpart detected by *Swift* in a 4.8 ks exposure is a dim object with 11 counts (R.A. =  $05^{\text{h}}23^{\text{m}}17^{\text{s}}.11$ ; decl. =  $-25^{\circ}27'31''.9$ ), not found in the UV band.

*J0803.2–0339*. Also, in this case only one X-ray source has been found (R.A. =  $08^{\text{h}}03^{\text{m}}12^{\text{s}}.11$ ; decl. =  $-03^{\circ}36'1''.4$ ) but at relatively high significance. The 80 counts detected in 3.9 ks were distributed following a power law of spectral index  $\Gamma = 2.10_{-0.31}^{+0.60}$ . *Swift* performed two observations on this object, and the light curve analysis shows some sign of variability ( $\sigma_{\text{var}} = 3.5$ ) with the count rate changing from  $0.018 \pm 0.003$  to  $0.039 \pm 0.005$ . Also, in this case no significant optical variability has been found in the two observations with the *W1* filter.

*J1036.1–6722*. The FOV of this source has been observed extensively (35.5 ks, spanning two years), but no bright X-ray sources have been detected. Only two marginal sources can be found above the  $3\sigma$  threshold: D1 (R.A. =  $10^{\text{h}}35^{\text{m}}45^{\text{s}}.98$ ; decl. =  $-67^{\circ}25'15''.4$ ) and D2 (R.A. =  $10^{\text{h}}36^{\text{m}}22^{\text{s}}.13$ ; decl. =  $-67^{\circ}22'28''.5$ ). The sources are very faint also in the UV band and are detected only at longer wavelengths because of the long exposures. Because of the low statistics, no variability analysis can be performed. The number of X-ray counts for the two sources is 34 and 10, respectively. But while in D1 the counts are evenly split below and above 1.5 keV ( $\Gamma = 1.9_{-0.8}^{+0.7}$ ), they are only in the soft band in D2.

*J1129.5+3758*. In four pointings (for a total of 4.8 ks), only two faint X-ray sources were detected: E1 (R.A. =  $11^{\text{h}}29^{\text{m}}03^{\text{s}}.42$ ; decl. =  $+37^{\circ}56'58''.6$ ) and E2 (R.A. =  $11^{\text{h}}29^{\text{m}}31^{\text{s}}.12$ ; decl. =  $+38^{\circ}01'59''.6$ ). The total counts are 11 and 10, distributed in a 2:1 ratio between the soft and hard band (HR =  $-0.3$  and  $-0.4$ ). Both sources are detected in the UV range.

*J1231.3–5112*. Also, in this case only dim objects were detected. F1 (R.A. =  $12^{\text{h}}31^{\text{m}}51^{\text{s}}.31$ ; decl. =  $-51^{\circ}19'39''.9$ ), F2 (R.A. =  $12^{\text{h}}30^{\text{m}}52^{\text{s}}.13$ ; decl. =  $-51^{\circ}19'17''.1$ ), and F3 (R.A. =  $12^{\text{h}}31^{\text{m}}29^{\text{s}}.62$ ; decl. =  $-51^{\circ}09'32''.3$ ) have 16, 5, and 15 counts observed in a 7.3 ks exposure. F1 is a hard source (HR = 0.25), while the other two sources have counts in the soft band only. While F1 and F2 have dim optical counterparts, F3 is a bright star, making this source an unlikely association of the  $\gamma$ -ray emission.

*J1844.3+1548*. Both the X-ray and UV analyses suggest that the likely counterpart of the  $\gamma$ -ray source is an AGN. The X-ray position (R.A. =  $18^{\text{h}}44^{\text{m}}25^{\text{s}}.42$ ; decl. =  $+15^{\circ}46'44''.3$ ) coincides with a known radio source (NVSS J184425+154646). The spectral analysis of the 4.2 ks exposure indicates a very steep photon index ( $\Gamma = 3.00_{-0.39}^{+0.42}$ ), an intrinsic absorption well above the Galactic value ( $n_{\text{H,Gal}} = 1.73 \times 10^{21}$ , and  $n_{\text{H,int}} = 2.63 \pm 0.06 \times 10^{21}$ ), and a 0.3–10 keV unabsorbed flux  $F_X = 9.5_{-3.2}^{+6.7} \times 10^{-12}$  erg cm $^{-2}$  s $^{-1}$ . The X-ray evolution indicates that the source count rate varied between  $0.110 \pm 0.007$  on 2011 November 18 and  $0.019 \pm 0.007$  on 2011 November 30,

and it remained constant at  $(0.020 \pm 0.006)$  on 2011 December 4. The UV light curve shows variation as well: in the *M2* filters the source brightness declined by a magnitude from the first ( $m_{M2} = 19.00 \pm 0.08$ ) to the last observation ( $m_{M2} = 19.99 \pm 0.25$ ).

#### 4.2. Radio Results

Seven of our 16 *Fermi* unassociated sources were observed over two epochs on 2012 August 27 and 2012 September 4. Altogether, a total of 13 radio pointings were required to observe all the possible X-ray counterparts.

Six of our seven *Fermi* sources were detected in at least one radio frequency at one of their X-ray candidate counterpart locations. The flux density of the sources detected ranges from 8 mJy to 97 mJy (sources B1 and F1, respectively) at 5.5 GHz. All the radio sources reported in Table 1 are within the  $1\sigma$  error ellipse of their corresponding X-ray source. Unique radio counterparts to the X-ray detection were found for the four sources (A1, C1, E1, G1) that were detected in multiple radio bands.

In the case of the sources J0523.3–2530 and J1036.1–6722, the error ellipse of our radio observation includes three discrete sources identified by earlier radio surveys. Thus, we cannot determine which of these three sources (or which two or all three) are being detected. Higher resolution observations and/or multi-epoch variability observations will be required to firmly establish the counterpart to these two *Fermi* candidates.

For J0143.6–5844 in addition to A1, two alternate nearby radio sources (A2 and A3) were detected with a much lower radio flux density, almost certainly because of the large beam<sup>14</sup> at 5.5 GHz. J1129.5+3758 was observed to have a flat spectrum between two observed frequencies (5.5 and 9.0 GHz). Observations at higher frequencies were not performed because of its low elevation at the ATCA, which would make such observations problematic. We will confirm that its flat spectrum extends to higher frequencies in future observations with a more northern telescope. The only  $\gamma$ -ray source where no radio sources were detected is J1231.3–5112, and an upper limit of  $\sim 10$  mJy at 5.5 and 9 GHz can be placed on all three radio pointings.

In follow-up observations on 2012 August 26 with the two element Ceduna Hobart Interferometer (CHI; Blanchard et al. 2012) that has a resolution of 6.6 mas at the observed frequency of 6.7 GHz, source A1 in J0143.6–5844 was detected with a flux density of  $25 \pm 4$  mJy. This compares to a flux density of  $26 \pm 3$  mJy measured by the ATCA at the adjacent frequency of 5.5 GHz. Thus, we conclude that J0143.6–5844 is a very compact object. CHI observations of the other detected sources are also planned.

An independent radio follow-up of unassociated 2FGL sources by Petrov et al. (2013) found the same candidate counterparts for J0143.6–5844 and J0803.2–0339 and confirmed our nondetection of J1231.3–5112.

## 5. DISCUSSION

### 5.1. AGN Candidates

In order to discuss the multiwavelength properties of the counterparts presented in the previous section, spectral energy distributions (SEDs) were built for the  $\gamma$ -ray sources where a radio counterpart was detected in at least two frequencies (2FGL J0143.6–5844, J0803.2–0339, J1129.5+3758, and

<sup>14</sup> While pointed at A2 and A3, the telescope is sensitive to flux from A1.

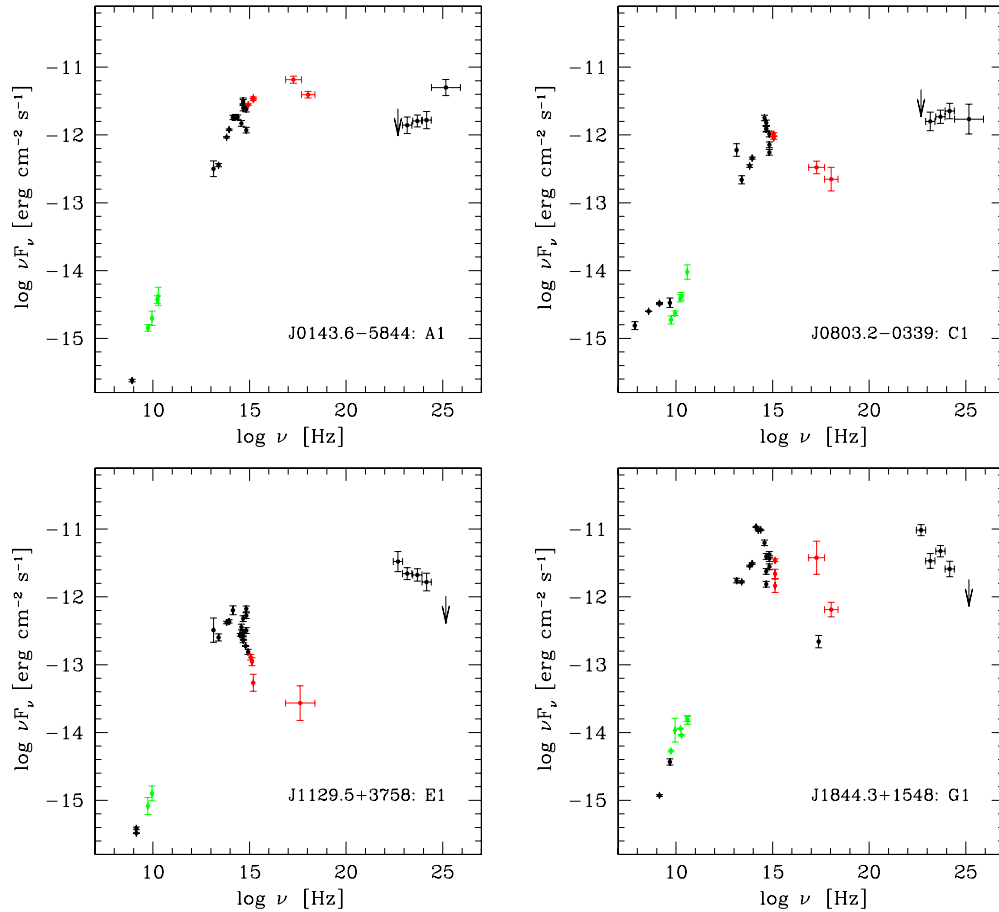


**Figure 2.** Spectral energy distributions of the likely counterpart to the  $\gamma$ -ray sources J0143.6–5844, J0803.2–0339, J1129.5+3758, and J1844.3+1548 (from top left to bottom right). The green and red points correspond to the ATCA and *Swift* data presented in this paper. The black points represent archival data and are not necessarily simultaneous.

(A color version of this figure is available in the online journal.)

J1844.3+1548), making these sources strong candidates to be AGNs. To generate the SEDs for each candidate, we used the ASDC SED Builder (Stratta et al. 2011), a web-based program developed at the ASI Science Data Center that combines data from several missions and experiments together with catalogs, archival, and proprietary data. We used fluxes from our radio campaign, as well as from the UVOT images and the XRT events. The optical/UV fluxes were corrected for Galactic extinction, while we used the unabsorbed X-ray flux in the 0.3–1.5 and 1.5–10 keV energy ranges (or 0.3–10 keV only for sources with a limited number of counts). In the case of J1129.5+3758, where no spectral information could be derived because of the low statistics, the X-ray flux was derived assuming an absorbed power law with an index of 2.0 (similar to what is observed for the other AGN candidates), and the value of the Galactic  $n_{\text{H}}$  along the line of sight was used. The SEDs are shown in Figure 2 and are discussed individually below.

It is interesting to note that Mirabal et al. (2012) assign probabilities of 0.962 and higher for these four objects to be AGNs. Using an improved version of their infrared colors prediction method, a list of new  $\gamma$ -ray AGN candidates is presented in Massaro et al. (2013). When a prediction is available, a comparison of the results is presented.

*J0143.6–5844.* Among these four sources, the SED of A1 (Figure 2, top right panel) most closely resembles what has been observed in other blazar candidates: there is a flat radio spectrum that rises to a peak in the UV/soft X-ray range and declines

in the X-rays. This might be interpreted as the synchrotron component of the emission observed in the high-peaked (BL Lacertae) blazars. The flat spectrum observed in the *Fermi* LAT data suggests that the high-energy photons belong to a different emission process, likely inverse Compton upscatter of photons either in the relativistic jets (synchrotron self-Compton) or from outside the jets (external Compton). Other supporting evidence is found in Massaro et al. (2013), where the infrared source WISE J014347.39–584551.3 (spatially coincident with the X-ray source A1) is classified as an AGN and more specifically as a BL Lac candidate.

*J0803.2–0339.* The combination of archival and new radio data might indicate that the source C1 has evolved with time, moving from a flat to a steep radio spectrum. However, these data are not simultaneous and should be interpreted with caution. This kind of behavior has been seen in other blazars (e.g., PKS 0521–36; Tornikoski et al. 2002) when the steep spectrum is seen during an active period. Furthermore, the observations of a steep radio spectrum in a quasar by LAT is not uncommon (Abdo et al. 2010b). The emission from radio to X-rays is again dominated by synchrotron radiation, although in the optical a sign of the contribution from the host galaxy is evident. Also, in this case the high-energy photons do not seem to be due to the same radiation mechanism and may be produced by inverse Compton upscattering. In addition, we note that the variability index reported in the 2FGL catalog for this source ( $\text{TS}_{\text{var}} = 48.58$ ; Nolan et al. 2012) indicates a  $\gamma$ -ray variability



with a  $>99\%$  confidence level<sup>15</sup>, supporting an AGN nature for this object. For this source, no  $\gamma$ -ray AGN candidate was found in Massaro et al. (2013).

*J1129.5+3758*. The SED of E1 is very puzzling; while the galaxy contribution is an evident feature in the near-IR to the UV, the radio, X-ray, and  $\gamma$ -ray emissions are more difficult to reconcile. The relatively steep spectrum in the GeV range and the very low value of the X-ray flux indicate that a peak of emission must be found between these two ranges. Considering that the hardness ratio in the X-rays is  $-0.3$ , this might indicate a somewhat flat spectrum and, consequently, that the X-ray emission might be produced by the same mechanism as the  $\gamma$ -rays. Unfortunately, the lack of a detailed X-ray spectrum does not allow us to draw a firm conclusion. In any case, the parabola that would fit the inverse Compton emission in the X-rays and the  $\gamma$ -rays would be very narrow. The radio emission, meanwhile, cannot be an extrapolation of the higher energy emission. If this counterpart is indeed a blazar, then the radio emission might be produced by synchrotron with a very low peak emission, particularly when compared with the inverse Compton peak. The ratio between the synchrotron and the inverse Compton peak might differ by a factor of 2–3 orders of magnitude, a relatively uncommon feature among blazars (see, e.g., Giommi et al. 2012). We also note that there is a hint of  $\gamma$ -ray variability in the aperture photometry light curve provided by the Fermi Science Support Center<sup>16</sup>. However, this variability is probably contamination from the nearby (angular separation of  $1\text{'}$ ) flaring  $\gamma$ -ray source 2FGL J1127.6+3622.

*J1844.3+1548*. The SED of G1 is another intriguing case; the near-IR to the UV is thermal radiation produced by the stars in the host galaxy. The very steep X-ray spectrum is a feature observed in narrow-line Seyfert 1 galaxies (NLSy1, see, e.g., Grupe et al. 2004, and references therein). In those objects, the steep spectrum may be due to intense soft X-ray flux cooling the accretion disk corona (Maraschi & Haardt 1997). The soft flux is not observed in this source because of the relatively high intrinsic absorption found in the X-ray analysis. If G1 is really an NLSy1, then it belongs to the rare class of radio-loud NLSy1 galaxies, a class that have been found to be a  $\gamma$ -ray emitter (Abdo et al. 2009; Foschini et al. 2011; D’Ammando et al. 2012). In these sources, the emission in the radio and the  $\gamma$ -ray is produced by a blazar-like relativistic jet that is dissipating most of its energy beyond the broad-line region (Ghisellini & Tavecchio 2008). We note that the infrared source WISE J184425.36+154645.9 (spatially coincident with the X-ray source G1) is also classified as a BL Lac candidate in Massaro et al. (2013).

### 5.2. Pulsar Candidate

*J1036.1–6722*. For this object, only two X-ray sources with significance  $>3\sigma$  are detected in a 35 ks observation, the deepest for our sample. Counterparts in the radio were found for only one X-ray source (D1) and were only detected at 5.5 GHz, indicating a steep radio spectrum. In  $\gamma$ -rays, the best-fit spectral model reported in the 2FGL is a LogParabola. In addition, no infrared AGN candidates are reported in Massaro et al. (2013) for this  $\gamma$ -ray source. Those characteristics are reminiscent of what is seen for the pulsar/MSP population observed with the Fermi LAT. This  $\gamma$ -ray source is therefore a prime candidate to

search for  $\gamma$ -ray pulsation at the position of the newly detected counterpart. The *much* reduced position error ellipse (from  $0\text{'}$ :1 to  $\sim 4\text{'}$ ) will allow exploration of the parameter space (e.g., pulsar period) in considerably greater detail. We note that in the case of a binary system, the measurement of the orbital period (through, e.g., optical observations) will greatly enhance the probability of detecting the pulsation.

### 5.3. Intriguing Objects

*J0523.3–2530*. Although J0523.3–2530 is the brightest  $\gamma$ -ray source in our sample, only one faint X-ray source was detected, with a radio counterpart only at the lowest radio frequency. While the radio, UV, and X-ray observations might suggest a pulsar origin, the  $\gamma$ -ray spectrum is best represented by a power law as seen for other AGN candidates. However, Massaro et al. (2013) report no AGN candidate for this source, and interestingly, the probability to be an AGN is  $P(\text{AGN}) = 0.738$  (Mirabal et al. 2012), a value that places this source neither in the pulsar nor in the AGN class.

*J1231.3–5112*. The two interesting X-ray counterparts (F1 and F2) have dim UV counterparts and no detection in the radio. This unidentified source has intriguing  $\gamma$ -ray properties, as the best-fit spectral model, a LogParabola, may suggest a pulsar origin while the light curve is not constant, with a  $\gamma$ -ray variability index of ( $\text{TS}_{\text{var}} = 39.04$ ; Nolan et al. 2012). As for the previous source, the probability to be an AGN is at an intermediate value,  $P(\text{AGN}) = 0.554$ .

Further radio and X-ray follow-up observations of these sources are therefore required to understand their nature.

### 5.4. X-Ray Chance Coincidence for Non-AGN Candidates

Although the X-ray to radio connection, combined with the detection of X-ray variability and the presence of a flat radio spectrum, is a step forward in pinpointing AGNs, a simple detection in the optical/UV/X-ray regimes is insufficient in determining the correct counterpart for pulsar-like  $\gamma$ -ray sources. For this category of sources, the probability of chance coincidence was investigated. Among the three non-AGN candidates, two of them (J0523.3–2530 and J1231.3–5112) had no *Swift* XRT detection outside the  $R_{95}$  error ellipse. The X-ray sources presented in Table 1 are therefore promising counterpart candidates. For J1036.1–6722, whose *Swift* exposure time was longer (35.5 ks, compared to a standard  $\sim 4$  ks for the other sources), 13 other sources were observed outside the  $R_{95}$  region. The majority (eight) of these sources have a detection significance just above  $3\sigma$ , and no additional information can be obtained. We tentatively tried to look for peculiar behaviors for the remaining five sources, whose detection significance is in the range  $4.5\text{--}6.3\sigma$ , by using the XRT and the UVOT data. The analysis of the 26 XRT observations does not show any sign of significant variability (above  $1\sigma$ ). Inspection of the five UVOT filters shows that of the five X-ray sources, one does not have any optical/UV counterpart, two have very weak counterparts, and the other two have strong counterparts. Unfortunately, we are not able to estimate the variability of the latter two sources, since they are located outside the UVOT FOV<sup>17</sup> most of the time. We estimated the chance coincidence of finding X-ray sources within the  $R_{95}$  region following the method explained in Bloom et al. (2002). The probability of chance association  $P$  can be expressed as  $P = 1 - e^{-A \times \rho}$ , where  $A$  is the area of the  $R_{95}$  region (a  $0\text{'}$ :062  $\times$   $0\text{'}$ :058 ellipse), while  $\rho$  is the sky

<sup>15</sup> In the analysis presented in the catalog, a  $\text{TS}_{\text{var}} > 41.60$  is used to identify variable sources at a 99% confidence level.

<sup>16</sup> [http://fermi.gsfc.nasa.gov/ssc/data/access/lat/2yr\\_catalog/ap\\_lcs.php](http://fermi.gsfc.nasa.gov/ssc/data/access/lat/2yr_catalog/ap_lcs.php)

<sup>17</sup> The UVOT FOV is  $17' \times 17'$ , while the XRT camera has a circular shape of  $12'$  in radius.



density of objects with equal or greater X-ray brightness. Since there are 15 sources in the XRT FOV (a circular shape  $12'$  in radius) detected above the  $3\sigma$  level (D2 in Table 1), the chance probability is 0.74.

While this value is high, D1 has a slightly higher chance to be the  $\gamma$ -ray counterpart than other X-ray detected sources because it is located within the  $R_{95}$  region, is the second brightest object in the XRT field, and is detected at 5.5 GHz. However, other sources detected in the XRT field can still be considered as candidates for the association.

## 6. SUMMARY AND CONCLUSION

We have used the combination of X-ray and radio follow-up observations to investigate the nature of a sample of bright, high-latitude 2FGL unassociated sources. X-ray observations from the *Swift* satellite were used to identify potential counterparts within the *Fermi* position error ellipse, which were then targeted with radio follow-up observations. The nature of the counterparts and their possible association with the  $\gamma$ -ray source were then discussed in a multiwavelength context. Out of the seven objects presented in this study, four  $\gamma$ -ray sources show a converging trend of evidence that suggests an AGN nature. Among those sources, J1844.3+1548 could be associated with an NLSy1, a rare class of  $\gamma$ -ray emitter. Although the limited sample was considered here, we note that X-rays are good tracers of potential AGN counterparts as, when a bright X-ray source was found in our sample, a radio flat spectrum counterpart was detected. Follow-up optical observations are planned to determine the redshift of those AGN candidates as well as to confirm the NLSy1 nature of J1844.3+1548. Our study confirms that the combination of X-rays and radio follow-up observations provides an efficient method to identify AGN candidates among the *Fermi* unassociated sources. It is also interesting to note that our list of AGN candidates constructed using multiwavelength properties is in agreement with the prediction, based on the GeV properties only, made by Mirabal et al. (2012).

The identification of candidates belonging to known classes of astrophysical objects narrows down the list of associated sources to the truly exotic objects. Additionally, the newly discovered members of known classes are also of great interest as they represent outliers in their respective classes. For example, our new candidate AGN (J1129.5+3758) may belong to a potentially important subclass: high Compton dominance AGN. Compton dominance is the ratio of the peak Compton to the peak synchrotron luminosity. The radio-weak,  $\gamma$ -ray loud AGNs we detect are increasing the size of this key sample, which can address the many questions that the relation of the Compton dominance to AGN properties like peak synchrotron frequency (Finke 2013) raise, e.g., the existence of the “blazar sequence” (Fossati et al. 1998).

The precise location of the putative counterpart of the pulsar candidate we have identified in our sample (J1036.1–6722), will be used to perform deep  $\gamma$ -ray pulsation searches. The improved location translates to a dramatic reduction in the volume of phase space that will need to be searched, making this task computationally more feasible.

In Su & Finkbeiner (2012), the line at 130 GeV (potentially resulting from dark matter annihilation) is investigated in a sample of *Fermi* unassociated sources, of which J1844.3+1548 is the brightest source. In this work we have demonstrated that this object is probably associated with an AGN and unlikely to be a signature of dark matter annihilation.

In our hunt to identify the truly “exotic” objects, we found an intriguing pair (J0523.3–2530 and J1231.3–5112) of  $\gamma$ -ray sources whose multiwavelength properties do not seem to fit in the pulsar or in the AGN category. Further investigation of those extraordinary sources could provide a pathway to the discovery of new types of  $\gamma$ -ray emitters.

This work made use of data supplied by the UK *Swift* Science Data Centre at the University of Leicester (Evans et al. 2009). The Australia Telescope Compact Array is part of the Australia Telescope National Facility which is funded by the Commonwealth of Australia for operation as a National Facility managed by CSIRO. This research was funded in part by NASA through *Fermi* Guest Investigator grants NNH09ZDA001N and NNH10ZDA001N. This research was supported by an appointment to the NASA Postdoctoral Program at the Goddard Space Flight Center, administered by Oak Ridge Associated Universities through a contract with NASA. This research has made use of data from the NASA/IPAC Extragalactic Database (NED, operated by the Jet Propulsion Laboratory, California Institute of Technology, under contract with the National Aeronautics and Space Administration); and the SIMBAD database (operated at CDS, Strasbourg, France). This research has made use of NASA’s Astrophysics Data System.

*Facilities:* ATCA, Fermi, Swift

## REFERENCES

- Abdo, A. A., Ackermann, M., Ajello, M., et al. 2009, *ApJL*, 707, L142  
 Abdo, A. A., Ackermann, M., Ajello, M., et al. 2010a, *ApJS*, 187, 460  
 Abdo, A. A., Ackermann, M., Ajello, M., et al. 2010b, *ApJ*, 720, 912  
 Ackermann, M., Ajello, M., Allafort, A., et al. 2011, *ApJ*, 743, 171  
 Ackermann, M., Ajello, M., Allafort, A., et al. 2012, *ApJ*, 753, 83  
 Blanchard, J. M., Lovell, J. E. J., Ojha, R., et al. 2012, *A&A*, 538, A150  
 Bloom, J. S., Kulkarni, S. R., & Djorgovski, S. G. 2002, *AJ*, 123, 1111  
 Cheung, C. C., Donato, D., Gehrels, N., Sokolovsky, K. V., & Giroletti, M. 2012, *ApJ*, 756, 33  
 D’Ammando, F., Orienti, M., Finke, J., et al. 2012, *MNRAS*, 426, 317  
 Dormody, M., Johnson, R. P., Atwood, W. B., et al. 2011, *ApJ*, 742, 126  
 Evans, P. A., Beardmore, A. P., Page, K. L., et al. 2009, *MNRAS*, 397, 1177  
 Finke, J. D. 2013, *ApJ*, 763, 134  
 Foschini, L., Ghisellini, G., Kovalev, Y. Y., et al. 2011, *MNRAS*, 413, 1671  
 Fossati, G., Maraschi, L., Celotti, A., Comastri, A., & Ghisellini, G. 1998, *MNRAS*, 299, 433  
 Ghisellini, G., & Tavecchio, F. 2008, *MNRAS*, 387, 1669  
 Giommi, P., Polenta, G., Lähteenmäki, A., et al. 2012, *A&A*, 541, A160  
 Grupe, D., Leighly, K. M., Burwitz, V., Predehl, P., & Mathur, S. 2004, *AJ*, 128, 1524  
 Kalberla, P. M. W., Burton, W. B., Hartmann, D., et al. 2005, *A&A*, 440, 775  
 Maraschi, L., & Haardt, F. 1997, in ASP Conf. Ser. 121, IAU Colloq. 163: Accretion Phenomena and Related Outflows, ed. D. T. Wickramasinghe, G. V. Bicknell, & L. Ferrario (San Francisco, CA: ASP), 101  
 Massaro, F., D’Abrusco, R., Paggi, A., et al. 2013, *ApJS*, 206, 13  
 Massaro, F., D’Abrusco, R., Tosti, G., et al. 2012a, *ApJ*, 750, 138  
 Massaro, F., D’Abrusco, R., Tosti, G., et al. 2012b, *ApJ*, 752, 61  
 Mirabal, N., Frías-Martínez, V., Hassan, T., & Frías-Martínez, E. 2012, *MNRAS*, 424, L64  
 Nolan, P. L., Abdo, A. A., Ackermann, M., et al. 2012, *ApJS*, 199, 31  
 Ojha, R., Kadler, M., Böck, M., et al. 2010, *A&A*, 519, A45  
 Petrov, L., Mahony, E. K., Edwards, P. G., et al. 2013, *MNRAS*, 432, 1294  
 Ray, P. S., Abdo, A. A., Parent, D., et al. 2012, arXiv:1205.3089  
 Romani, R. W. 2012, *ApJL*, 754, L25  
 Stevens, J., Edwards, P. G., Ojha, R., et al. 2012, arXiv:1205.2403  
 Stratta, G., Capalbi, M., Giommi, P., et al. (on behalf of the ASDC team) 2011, arXiv:1103.0749  
 Stroh, M. C., & Falcone, A. D. 2013, *ApJS*, 207, 28  
 Su, M., & Finkbeiner, D. P. 2012, arXiv:1207.7060  
 Tornikoski, M., Lähteenmäki, A., Lainela, M., & Valtaoja, E. 2002, *ApJ*, 579, 136